Edinburgh Research Explorer

Tomographic imaging of the liquid and vapour fuel distributions in a single-cylinder direct injection gasoline engine

OPEN ACCESS

Tomographic imaging of the liquid and vapour fuel distributions in a single-cylinder direct injection gasoline engine

Nataša Terzija[a1], Solon Karagiannopoulos[a], Steven Begg[b],
Paul Wright[a], Krikor Ozanyan[a] and Hugh McCann[c]

[a] School of Electrical and Electronic Engineering, University of Manchester, Manchester M13 9PL, UK
[b] Sir Harry Ricardo Laboratories, University of Brighton, Brighton BN2 4AT, UK
[c] School of Engineering, University of Edinburgh, Edinburgh, EH9 3JL, UK
[1] Now at Elektronische Fahrwerksysteme GmbH, Despag-Straße 3, D-85055 Ingolstadt, Germany

ABSTRACT

This paper reports the application of optical tomography and Chemical Species Tomography (CST) to the characterisation of the in-cylinder mixture preparation process in a gasoline, direct injection, single-cylinder, motored research engine. An array of 32 near-infrared beams are transmitted in a horizontal plane across the cylinder bore near the top of the cylinder, through a circular quartz annulus. A novel approach to enable the optical alignment of the transmitting and receiving optics is utilised. The engine is operated at a stoichiometric condition at 1200 rpm, with negative valve overlap timing. Two tomographic measurement schemes (optical attenuation and chemically specific absorption) were used to acquire data on the spatial and temporal distribution of fuel throughout the engine cycle. Optimised data pre-processing methods are described for maximal beam count and data reliability. The presence of fuel during the intake stroke was detected by the optical beam attenuation due to scattering from the liquid gasoline droplets. Optical tomographic reconstruction of the spatial distribution of these droplets was achieved at an imaging rate of 7,200 frames per second (fps), revealing rapid intra-cycle spatial variations that were consistent between consecutive cycles. During the compression stroke, CST images of fuel vapour were reconstructed from data acquired using chemically-selective spectral absorption by the hydrocarbon (HC) molecules, at an imaging rate of 2,400 fps. Late in the compression stroke, the temporal evolution of the fuel vapour distribution in the plane of observation is relatively slow, and displays inhomogeneities that are consistent between consecutive cycles. This is the first report of the use of tomography to image, within individual engine cycles, the in-cylinder evolution of both fuel spray droplet distribution and fuel vapour distribution.

Keywords Optical tomography, chemical species tomography, direct injection, engine, fuel, spray, vapour, mixture preparation

1   INTRODUCTION

The internal combustion engine will remain a viable and integral part of power sources for many mobile and fixed applications in the foreseeable future. To date, the most technologically advanced of these is the gasoline direct injection (GDI) combustion system that has been shown to offer a significant reduction in fuel consumption and exhaust emissions, comparable with the efficiencies and power output of the best Diesel and hybrid systems [1, 2]. However, the lean mixture combustion modes employed in such engines are sensitive to variations in the air-fuel concentration and mixture and thermal distributions in the cylinder that are manifested as fluctuations in the engine performance from one cycle to the next [3, 4]. The effect is more pronounced at low engine speeds and loads, where the mixing gas velocities are reduced, and for lean operation, where inadequate mixture preparation and low temperatures can result in misfires. Fundamental knowledge of these processes is necessary in order to model, develop and implement robust combustion control strategies for engine management. Therefore, there is a requirement to image the entire process of fuel preparation within individual engine cycles, and over many consecutive cycles. This target demands that, for each individual cycle, the development of the fuel distribution is imaged continuously, i.e. from the early liquid spray-dominated stages to the late stages of the vapour-dominated mixing and evaporation processes immediately prior to ignition. In turn, the dynamic nature of these processes places great demands upon temporal resolution of the imaging system. This is discussed in greater detail in Section 2, showing that the previous state-of-the-art has achieved limited success in attempting to image the continuous development of fuel distribution through all of the above stages within an individual engine cycle and from cycle to cycle.

1

We report here the application of an optical tomography system in a single-cylinder research engine to address the above challenge, i.e. to image continuously, at a high frame rate, within individual engine cycles and continuously over many consecutive cycles, the following stages:

(a) the gross distribution of liquid spray at fuel injection and over the evaporation phase

(b) the fuel vapour distribution in the compression stroke, up to the time immediately prior to piston obscuration of the optical beams across the cylinder.

The opto-electronic system used was previously reported in [5], along with its application to stage (b) above, in a Ford Duratec in-line 4-cylinder Port-Fuel-Injected (PFI) engine. Whilst the work reported in the present paper did not use the bespoke system for optical access and optical transmission (launch) and receive reported in [5], the remainder of the system is still referred to here by the name *IMAGER*. The *IMAGER* electronics was designed from the outset to cope with the effects of fuel sprays upon the low-frequency properties of the received light from each beam, which have been discussed in [6], and the present paper describes the first application of *IMAGER* to a GDI engine.

In this paper, Section 2 outlines the essential features of tomography and of the *IMAGER* system, relevant to this study, and the physical basis underlying the data analysis. Section 3 describes the engine specification. Section 4 discusses the novel optical mounting and alignment methods used to launch 32 beams through the optical cylinder liner and through the air/fuel charge inside the cylinder. Section 5 discusses the behavior of individual beam data. Reconstructed image data are presented in Section 6. Discussion and interpretation of the images then follow in Section 7 and a summary of conclusions is presented in Section 8.

2   IN-CYLINDER FUEL IMAGING METHODS

General background

There is an extensive literature concerned with tools and techniques related to in-cylinder imaging of liquid and vapour fuel. From a review of the literature with an emphasis upon the demands of GDI engine research, the optimal method for in-cylinder imaging of fuel distribution should take into consideration the following guidelines:

(1) non-intrusive to in-cylinder flow and combustion processes;
(2) responsive to individual fuel droplets in the injector spray;
(3) sensitive to the size distribution of the above fuel droplets;
(4) sensitive to the fuel in both liquid- and gas-phase;
(5) capable of (4) above without the use of artificial dopants, i.e. directly sensitive to the fuel;
(6) capable of imaging real multi-component road fuels as well as single-component reference fuels;
(7) sensitive over a wide dynamic range of gaseous fuel concentration, from hundreds of parts per million by volume (ppm) to tens of thousands of ppm;
(8) capable of spatially resolving all in-cylinder flow scales, i.e. from about droplet size up to large fractions of the cylinder diameter (D);
(9) capable of providing continuous sub-cycle images with temporal resolution equivalent to intervals between images of about one degree of crank shaft rotation (ºCA);
(10) in the case of gas-phase measurement, robust against non-species-specific optical effects, such as Mie scattering;
(11) robust against the hostile thermodynamic environment of the engine;
(12) applicable to specialised single-cylinder research engines and also to multi-cylinder engines with minimal engine modification;
(13) free of potential additional hazards beyond those inherent in the engine test cell environment.

To date, no technique has been shown to satisfy all of the above requirements. However, several optical methods have been developed that offer partial solutions, as discussed and reviewed by many authors, e.g. [7-9], and have been widely exploited by combustion researchers [10] and by engine and fuel product developers [11]. These methods exploit a wide range of phenomena, from Mie scattering to chemically sensitive spectroscopic techniques.

For in-cylinder gaseous species imaging, Planar Laser-Induced Fluorescence (PLIF) has become a commonly used method and it has been widely used for studies of fuel-air mixture preparation and combustion processes for over 25 years, as reviewed in detail in [8]. PLIF provides excellent spatial and temporal resolution (sub-mm and sub-ms, respectively), and recent advances in both lasers and direct imaging detectors enable continuous imaging over many cycles [9]. These capabilities come at the cost of considerable engineering complexity. In particular, planar optical access is required along two perpendicular axes and quantification of the received signals from hydrocarbon fuels requires the use of model fuels only and the introduction of fluorescent dopants. In addition, the choice of dopant, its concentration in the base fuel, in-cylinder gas pressure, temperature and oxygen concentration (a feature pertinent to lean burn engines) are all known to influence the fluorescence signal. As a result, the PLIF technique is not readily applicable in a quantitative manner for commercial multi-component fuels and real multi-cylinder engines.

As reviewed in [7], many authors have studied sprays in the laboratory environment, using a range of sophisticated techniques, but attempts to transfer them to operating engines have proved very difficult. Off-engine studies in constant-volume chambers, such as that by Nishida et al. [9], have attempted to recreate many of the conditions encountered in engines. The two main methods that have been applied in-cylinder to operating engines are:

(i) high-speed video of Mie-scattered light from sprays, illuminated by sources such as copper-vapour lasers or high-intensity discharge lamps [13, 14]

(ii) Laser-Induced Exciplex Fluorescence (LIEF) [15-17], the principle of which has been summarised in [7].

As shown in [14] by its application in a square-piston engine, method (i) is capable of very high imaging rates, viz. 9,000 fps, and excellent spatial resolution (10 μm/pixel), thus revealing the complexity and subtlety of cycle-to-cycle variations in fuel injection spray behaviour. That very phenomenon begs for the capability to follow each spray event into the later stages of mixture preparation, but method (i) does not satisfy this need.

Since LIEF was initially described by Melton as a technique for Diesel sprays [15], it has also been used in gasoline engines by various researchers, e.g. [16, 17], exactly because of its ability to image both liquid- and gas-phase constituents. Therefore, LIEF does indeed offer the prospect of imaging the spray-dominated stage as well as the gas-dominated stage of the GDI mixture preparation process, within a given engine cycle. In addition to the complexities noted above in PLIF imaging of gas-phase systems, the LIEF variant has the added difficulties of multiple dopant species, e.g. absolute liquid phase concentration measurement requires detailed knowledge of the temperature-dependent spectral emission from the exciplex dopants in the spray. Leach et al. [17] applied LIEF to a motored GDI engine, with images taken at up to 2,400 fps with spatial resolution of 200 μm/pixel, and discussed the difficulty of eliminating "cross-talk", whereby the fluorescence signal from one phase may be mistakenly attributed to the other. By averaging over 20 cycles, partly to overcome high shot-to-shot variation in laser power, these authors achieved a qualitative analysis of the mean behaviour of liquid- and gas-phases, but did not demonstrate the following of fuel from liquid- to gas-phase within a single cycle, or the effects of cycle-to-cycle variation. Using LIEF in a constant-volume chamber study that is particularly relevant to the GDI engine case, and exploiting a dopant system that had only recently been spectrally characterised, Fansler et al. [18] achieved a fully quantitative analysis of evaporating sprays, with particular emphasis on the stage where liquid- and gas-phase coexisted in the spray region.

Tomographic techniques

The method of Near Infra-Red Absorption Tomography (NIRAT) for in-cylinder gaseous fuel imaging has previously been applied by the authors to a multi-cylinder engine [5], in a form whereby it is chemically selective specifically to long-chain hydrocarbon molecules. However, as pointed out in [6], optical tomography in non-chemically selective form also has the potential to image the in-cylinder spatial distribution of sprays. In this paper, we present the combination of those two approaches. Significantly, the requirement for optical access in only a single plane should allow the use of optical tomography at all stages of the product development process, from initial flow bench studies, through single-cylinder engine tests, to final design validation in multi-cylinder implementations. Moreover, the

fact that optical tomography, including its chemically specific variants, does not depend on artificial dopants introduced into the fuel promises considerable logistical convenience, particularly for application to commercial multi-component fuel mixtures.

A brief literature review of chemically-selective optical tomography has been presented in [5]. Further work relevant to in-cylinder engine application has been published recently by Sanders et al. [19]. The basic principle of the method used in *IMAGER* is recapped here. To exploit the infra-red absorption spectroscopy of a target molecule, a wavelength λ is chosen, corresponding to a particular absorption feature with known spectroscopic properties. According to the Beer-Lambert law, eq. (1), the intensity, $I_r(\lambda)$, of light received on a photodetector transmitted over a path of length L through a gaseous cloud containing a target species of spatially varying concentration c is given by:

$$I_r(\lambda) = I_O(\lambda)\exp\left(-k(\lambda)\int_L c\,.dl\right) \tag{1}$$

where $I_o(\lambda)$ is the incident light intensity, $k(\lambda)$ is the wavelength-dependent absorption coefficient for the target species, and dl is the line element along the beam path. By measuring the attenuation over enough co-planar but angularly distributed paths through the subject, the concentration distribution c in the plane can be reconstructed by well-established methods, e.g. see [20]. All of the optical launch and receive elements are therefore in a single plane, overcoming one of the major engineering challenges in PLIF and other imaging techniques.

In the absence of any other attenuation mechanisms, the quantity that must be determined in order to carry out tomographic reconstruction is the line integral in eq. (1), termed the path-concentration integral (PCI). Given that other non-species-specific attenuation mechanisms (e.g. scattering) normally occur, it is necessary to isolate the PCI of the attenuation due only to spectroscopic absorption by the target species, which is achieved by taking the ratio of transmission of an absorbed wavelength λ_1 to that of a non-specifically absorbed (reference) wavelength λ_2, as shown below:

$$\int_L c\,.dl = \frac{1}{k(\lambda_1)-k(\lambda_2)}\ \ln\left(\frac{I_r(\lambda_2)}{I_r(\lambda_1)}\,.\frac{I_O(\lambda_1)}{I_O(\lambda_2)}\right) \tag{2}$$

The value of $k(\lambda_2)$ in the present work is negligible. This method of measuring the PCI due only to absorption by molecules of the target species is called the Dual-Wavelength Ratio (DWR) method. The PCI measurements that underlie tomography are able to be calibrated, thus underpinning images that are fundamentally quantitative in nature, in terms of species concentration. For the case of in-cylinder chemical species tomography (CST) of fuel, equ. (2) is developed in more detail below.

In *IMAGER*, λ_1 is chosen to be 1700 nm, which is absorbed by vibrational transitions of the C-H bond in large hydrocarbon (HC) molecules, and is thus sensitive to any such molecule in normal HC fuel, without the requirement to add dopant species. This absorption feature of long-chain hydrocarbons is very broad (~15 nm half-width at half-maximum) and unstructured, as discussed in [21], when compared with the very narrow spectral width of the diode laser sources used, and when compared with the sub-nm width of absorption features of small molecules that are typically measured in tunable diode laser absorption spectroscopy (TDLAS) systems [22]. The spectral absorption properties of air/HC fuel mixtures are relatively easy to calibrate in terms of temperature and pressure, as reported in [21, 23]. For a stoichiometric mixture of air and iso-octane, at about 10 bar pressure in a typical gasoline engine cylinder, a beam of light at 1700 nm passing diametrically through the cylinder will undergo around 5% absorption by HC molecules. The reference wavelength, λ_2, is chosen to be 1651 nm, and both wavelengths are provided by diode lasers. The measurement of the transmitted intensity at each of the two wavelengths is performed simultaneously using a dual-frequency lock-in technique, described in detail by Wright et al. [5]. The PCI measurement for each beam is performed and recorded at high speed, 100 kilosamples/s (kS/s), but subsequent filtering typically reduces the imaging rate, e.g. to 3,000 fps [5]. The system can gather measurement data at 100 kS/s continuously on 32 beams for many minutes, limited by the memory capacity of the data logging system. More limiting is that, by using individual fibres and collimators, optical mounting requirements around the engine cylinder dictate that only a few tens of distinct PCI measurements can be obtained, which is challenging in terms of image reconstruction. Extensive development of image reconstruction methods and robust laboratory tests of *IMAGER* [23, 24] demonstrated its fundamental imaging

4

capability, with spatial resolution about 4% of the subject cross-sectional area, which is clearly much poorer than PLIF.

Using measurements of attenuation at only the reference wavelength λ_2 offers the prospect of imaging the distribution of scattering centres during the spray phase of the fuel preparation process [6]. Specific to the GDI case, Nishida et al. [9] have provided an analytical approach to a 2-wavelength large-diameter, single-beam transmission system in a constant-volume chamber, using p-xylene as a surrogate for gasoline due to its convenient absorption properties. Consistent with the experimental data of [6], they assumed that the reference wavelength intensity was attenuated only by scattering. They succeeded in imaging, in one projection plane parallel to the injector axis, the separate distributions of fuel in liquid- and gas-phases, having used the mass injection rate curve to achieve excellent quantification.

Physical basis of tomographic data analysis methods

For the case of in-cylinder CST of fuel, equ. (2) is developed in more detail here. Strictly speaking, the exponents in equations (3) – (7) ought to be expressed as path integrals, as in equ.(1) above. For clarity of understanding, they are presented below in a simpler form where the concentrations c are average values along the beam path. Under fuelled conditions (denoted by the subscript $_F$) the normalised *IMAGER* output signal at the measurement wavelength ($S_{\lambda 1}$) is given as a function of crank angle (θ) by

$$\left[S_{\lambda_1}(\theta)\right]_F = e^{\alpha_{1\theta ref}-\alpha_1(\theta)}.e^{\{kcl\}_{F\theta ref}-k(\theta).c_F(\theta).l} \tag{3}$$

where the first exponential term represents the normalised non-species-specific wavelength dependent attenuation $\alpha_1(\theta)$, due to scattering, beam deflection, etc., and the second exponential term represents the normalised species-specific wavelength-dependent molecular absorption derived from the Beer Lambert Law with crank angle- (pressure-) dependent absorption coefficient $k(\theta)$, path length l and crank angle-dependent fuel concentration $c_F(\theta)$. To ensure that any cycle-to-cycle variation in the DC signal level is removed from the optical signals $S_{\lambda 1}(t)$ and $S_{\lambda 2}(t)$, an intra-cycle reference crank angle interval is defined and indicated by θ_{ref}. The choice of θ_{ref} is discussed in section 5. The above treatment of the first term in exponential form is a departure from the previous practice in [5, 21, 23], and is found to be helpful below. Both terms are explicitly stated in terms of their deviation from their values at θ_{ref}. For the case of iso-octane/air at these pressures, it has been shown previously [21] that the temperature dependence of k is negligible.

The normalised signal at the reference wavelength ($S_{\lambda 2}$) is given as a function of θ by:

$$\left[S_{\lambda_2}(\theta)\right]_F = e^{\alpha_{2\theta ref}-\alpha_2(\theta)} \tag{4}$$

with only the non-species-specific wavelength dependent attenuation term $\alpha_2(\theta)$, due to scattering, beam deflection, etc., since there is no molecular absorption at this wavelength.

The Dual-Wavelength Ratio, R_F, of these two signals is given by:

$$\left[\frac{S_{\lambda_1}(\theta)}{S_{\lambda_2}(\theta)}\right]_F = R_F(\theta) = e^{\left(\alpha_{1ref}-\alpha_1(\theta)\right)-\left(\alpha_{2ref}-\alpha_2(\theta)\right)}.e^{\{kcl\}_{Fref}-k(\theta).c_F(\theta).l} \tag{5}$$

R_F is dependent upon both non-species-specific and species-specific attenuation of the beam; ideally, the non-species-specific attenuation would be non-wavelength-dependent and non-crank angle-dependent, but this formulation allows analysis of both of those conditions.

As discussed in Wright et al. [5], it is necessary to implement an additional inter-cycle referencing scheme to remove effects due to cylinder pressure and other phenomena that cyclically distort the optical system. This is achieved by making measurements under unfuelled conditions (denoted by the subscript $_{UF}$). Assuming that the crank angle dependence of in-cylinder pressure and temperature are identical in both the fuelled and the unfuelled cases, then under unfuelled conditions the Dual-Wavelength Ratio R_{UF} is given by:

$$R_{UF}(\theta) = e^{\left(\alpha_{1ref}-\alpha_1(\theta)\right)-\left(\alpha_{2ref}-\alpha_2(\theta)\right)}.e^{\{kcl\}_{UFref}-k(\theta).c_{UF}(\theta).l} \qquad (6)$$

Normalising the signals to a point of low absorption at the intra-cycle referencing stage such that

$$\{kcl\}_{Fref} = \{kcl\}_{UFref}$$

and assuming zero fuel concentration during unfuelled cycles, ensures that the ratio R_F/R_{UF} is dependent only on the fuel concentration during the fuelled cycles, i.e. it is given by:

$$\frac{R_F(\theta)}{R_{UF}(\theta)} = e^{-k(\theta).c_F(\theta).l} \qquad (7)$$

The empirical behaviour of (R_F/R_{UF}) is discussed in Section 5. For vapour imaging in the present study, the small values of the exponent in equ. (7) result in the following expression for the PCI:

$$PCI(\theta) = (1 - \frac{R_F(\theta)}{R_{UF}(\theta)})/k(\theta) \qquad (8)$$

3   Engine configuration and operating conditions

The work reported here uses a Ricardo Hydra, four-stroke, single-cylinder research engine, with a cylinder bore of 80 mm, stroke length 89 mm and compression ratio 9:1. The engine cylinder head was a single-cylinder direct injection type, supplied by the Orbital Engine Corporation. It featured a pent-roof combustion chamber with four valves, flat piston and a vertical, centrally located, air-assisted injector and spark plug. The air delivery absolute pressure was 6.5 bar and the fuel gauge pressure was 8 bar. The steady state region of the injector mass flow delivery rate was measured to be approximately 3.6 mg/ms. The poppet valves were actuated via double overhead camshafts with maximum valve lifts of 4 mm. The fuel used was a mixture of iso-octane (90% by volume) and 3-pentanone (10%). Further details of the engine specification are given in [17]. The direct injection engine was operated under motored conditions with a wide-open throttle, homogeneous, stoichiometric mixture preparation strategy. In the remainder of this paper, all crankangle positions are defined as follows: 0 degrees of crank angle rotation (ºCA) is at the start of the intake stroke, i.e. at non-firing Top Dead Centre (TDC); 360 ºCA is at the end of the compression stroke (where the second TDC of the cycle occurs); the complete cycle is 720 ºCA in duration. For clarity of discussion, the following text occasionally refers to positions after TDC (ATDC) or before TDC (BTDC), i.e. relative to 0 ºCA.

Experimental considerations for engine operation

For the tomographic imaging study in the optical engine, intake gas heating was used to mitigate the effects of motored operation, to increase the mean in-cylinder gas temperatures and to promote rapid and complete evaporation of the air-fuel mixture during the latter stages of the compression stroke. A high level of residual mixture (air and fuel) trapping and intake gas mixing turbulence were achieved by the use of early exhaust valve closure and late intake valve opening (negative valve overlap approach, NVO) resulting in low maximum valve lifts for short valve opening periods; the exhaust valves closed at 80 ºCA BTDC on the exhaust stroke and the intake valves opened at 90 ºCA ATDC. As such the in-cylinder pressure trace recorded two pressure peaks, the main peak occurring at firing TDC.

To facilitate the development of a homogeneous fuel-air mixture, fuel injection was timed 'early', nominally at 120 ºCA ATDC. However, a delay of approximately 1.3 ms occurred between the start of the electrical pulse to the injector and the observation of the start of liquid injection into the chamber, as reported in Leach et al. [17]. The engine was motored on a dynamometer at an engine speed of 1200 rpm. Engine speed, timing of control signals and synchronisation with the tomographic system was achieved using a high resolution rotary encoder coupled to the engine crankshaft and a once-per-revolution camshaft wheel sensor. The engine intake air was heated to greater than 70 ºC to compensate for the residual gas trapping and further increase vaporization of the fuel charge during gas compression. The coolant was maintained at a temperature of 90 ºC and the oil lubricant at a temperature of 40 ºC. The testing period typically varied between 1 to 5 minutes. Data from the optical

measurement array (see Fig. 2) were recorded for continuous periods of one minute; during each 1-minute period, the engine was operated with continuous fuelling for three equal sub-periods that corresponded to 16 consecutive engine cycles.

Transmitting and receiving setup

In this study a new system was designed and manufactured to enable the insertion of the optical annulus between the cylinder head and the cylinder block. This section of the cylinder liner was manufactured from fused silica that enables transmission of near-IR beams through the fuel-air charge. The 10 mm high optical annulus, manufactured to tolerance specification by Gooch and Housego Ltd. (Illminster, Somerset, UK), was mounted between the cylinder head and cylinder block as shown in Fig. 1. To attain satisfactory alignment between the transmitting and receiving optical elements (discussed in Section 3), it was necessary to maintain a form tolerance of 50 micrometres on each of the inner and outer diameters of the optical annulus, and a tolerance of 50 micrometres on their concentricity.
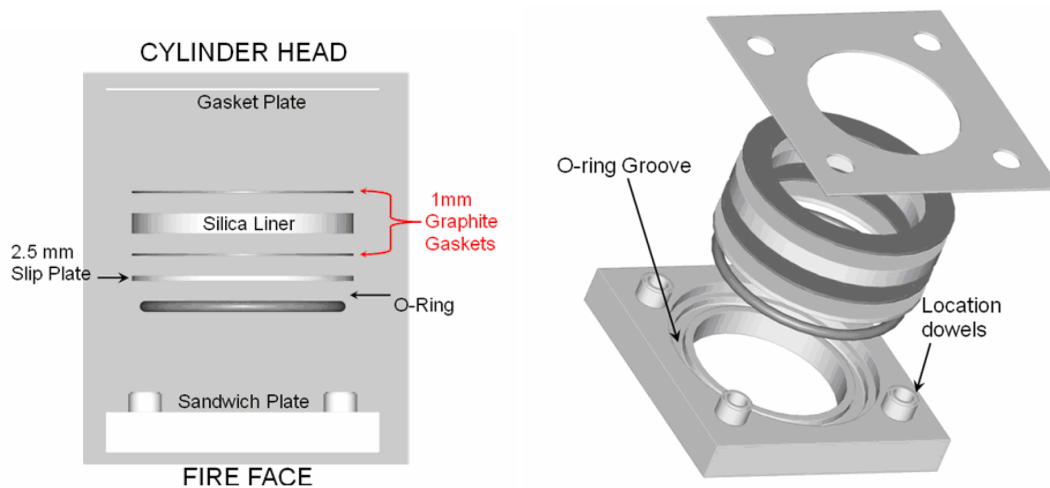

Figure 1: Schematic of the optical liner installation, (a) section view, and (b) perspective view.

4   Optical configuration of tomographic system on the engine

The array of 32 Near-IR beams was mounted in a horizontal plane 6 mm below and parallel to the fire-face of the cylinder head, to ensure that the optical path could not be blocked by the low-lift valves that were used. The optical transmission (launch) and receive optics are gradient-index (GRIN) lenses mated up with optical fibres that are connectorised at the opto-electronic interface end and supplied as robust bespoke assemblies (Grintech GmbH, Jena, Germany). Each ferrule containing the lens and fibre end is laid into an accurately machined V-groove in a flat optical plate that is mounted outside the optical liner and accurately positioned with respect to the liner by the location ring dowels shown in Fig. 1. To determine the positions of the array of V-grooves, sequential ray tracing was used to calculate the necessary ray paths outside of the cylinder liner such that, following refraction by the liner, a regular array of four projections, each with eight beams, was formed within the cylinder. The V-grooves were CNC-milled into a single plate of aluminium machined to fit around the optical liner during assembly of the cylinder head, as shown in Fig. 2.

As discussed in section 2, the *IMAGER* opto-electronic system [5] was used to conduct the experiments, providing light at both the HC-absorbed wavelength and the non-specifically absorbed wavelength to each of the 32 optical launch elements. *IMAGER* is designed to cope with the measurement of HC fuel vapour in the presence of high concentrations of scattering particles, by using intensity modulation of the two laser diode sources (300 kHz and 500 kHz), followed by dual-frequency demodulation of the signal from each of the 32 photodiodes. Data were streamed from the electronic system to hard disk storage, synchronously with TTL pulses from the once-per-cycle camshaft encoder.
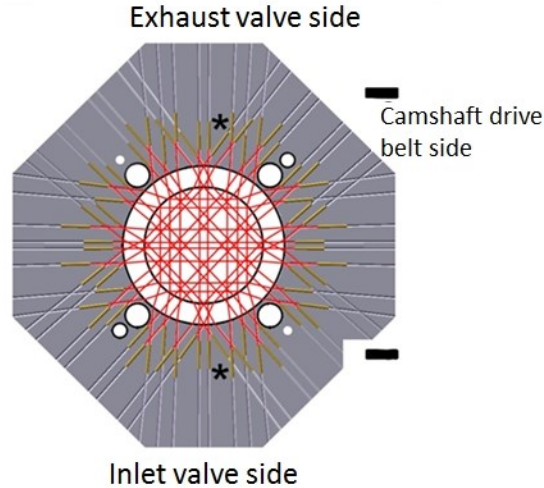
Figure 2: Plan view of 32-beam array mounted on the engine showing grooved plate and beam paths relative to intake and exhaust ports and camshaft (* denotes the example beam referred to in Figs. 3, 6, i.e. the vertical beam immediately to the left of the * symbol).

5   Time-series analysis of individual beam data

Recorded Data

In Fig. 3, example data from a typical short series of engine cycles are presented, showing the variation in the received optical intensity at the reference wavelength from a near-diametric beam (denoted by * in Fig. 2) running between the exhaust and inlet ports in the path of the injected fuel . In addition, the figure is overlaid with several further items of information: the TDC locations; the strokes within the 4-stroke cycle; the period of nominal Inlet Valve Opening (IVO) to Inlet Valve Closing (IVC); and the timing of the electrical trigger pulse to the fuel injector. Note that the beams are blocked when the top of the piston passes through the plane of the array at around 20 °CA either side of each TDC location. Attenuation of the beam by the injected fuel spray can clearly be seen in the optical signal shortly after the fuel injection trigger signal at 120 °CA ATDC. Note that the electrical delay due to the injector driver and the fuel spray transit time to the measurement location, means that the first observed fuel signal occurs at ~130 °CA ATDC. For the engine conditions tested at 1200 rpm, liquid fuel injection takes place over approximately 4.2 ms. Fuel evaporation can occur for a further 30 ms up to the ignition angle in the compression stroke. Continued signal attenuation can be seen throughout the intake stroke as the air flow distributes the fuel charge around the cylinder. For the heated intake gas condition tested, it can be seen in Fig. 3 that the majority of the liquid fuel has evaporated (early) by approximately 220 °CA ATDC. These features are discussed in more detail below.

Fig. 3 also shows the parts of the engine cycle where different types of data analysis are subsequently performed:

- images of the fuel spray distribution during injection and throughout the remainder of the intake stroke (100 to 200 °CA ATDC) were reconstructed using only the extinction of the optical signal received at the reference wavelength ($S_{\lambda 2}$), as in [6].

- images of the distribution of fuel vapour during the compression stroke (200 to 340 °CA ATDC) were reconstructed using PCI measurements derived by the DWR approach [5, 21, 23] as discussed in Section 2, using the signals at both the measurement ($S_{\lambda 1}$) and reference ($S_{\lambda 2}$) wavelengths, 1700 nm and 1651 nm respectively.

Data filtering and denoising

In the first step of the analysis, using the crankshaft encoder pulses, the time series data were referenced to crank angle and reshaped from a continuous stream to a series of arrays with each
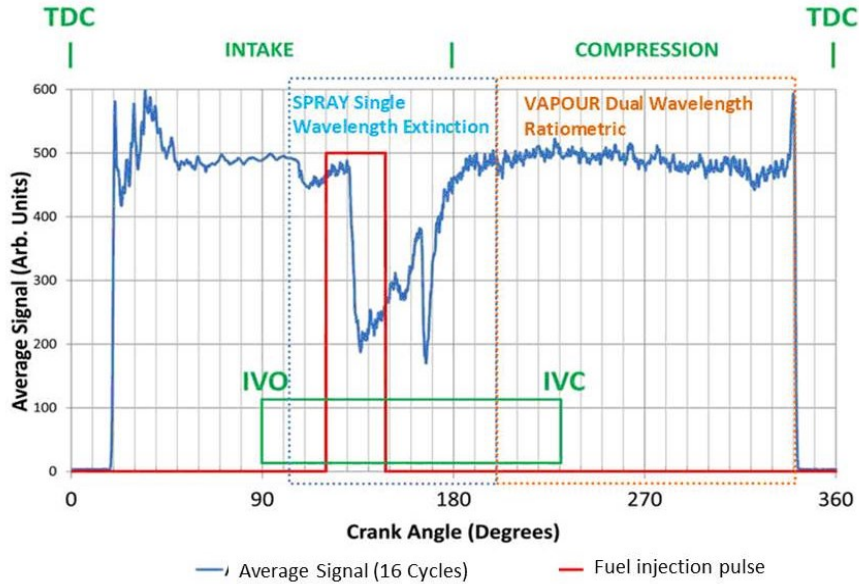
8

Figure 3: Average recorded signal intensity for 16 fuelled cycles for the selected example beam (reference wavelength) during the intake and compression strokes and engine cycle events.

array containing the data from each successive complete 4-stroke engine cycle (720 ºCA). In addition, the data were time-averaged to yield a temporal resolution equivalent to 1 frame per ºCA; at 1200 rpm this corresponds to a sample rate of 7.2 kS/s which is well within the bandwidth limit imposed by the system hardware.

As has been discussed extensively by Wright et al. [5], a number of mechanisms affect the behaviour of the individual beam measurements, in addition to scattering from spray droplets and chemically specific absorption, including malfunction or distortion of the beam optics. It is essential to identify and eliminate any beam data that do not behave in a physically sensible manner, but this can be challenging where there is also significant noise or other contributions to rapid data variation. On the other hand, it is essential for reliable tomographic image reconstruction that as many beams as possible are retained in the process. Hence the judgement of beam data quality is critically important. For this purpose, Wavelet Denoising (WD) [25, 26] is applied to the 1-D data stream of each individual beam, to enable a robust assessment of the behaviour of the beam data over the whole engine cycle or within one stroke of the engine cycle.

The WD procedure can be described by 3 main steps:
- multi-level decomposition to approximation and detail coefficients using the Discrete Wavelet transform;
- thresholding of the detail coefficients;
- wavelet reconstruction using the Inverse Discrete Wavelet transform.

To perform the wavelet decomposition the Daubechie filter db4 [27] was chosen and each signal was decomposed into 7 levels. A range of standard threshold techniques were tested in the MATLAB environment; the best denoising performance was obtained with the "mini-maxi threshold" [28]. Two examples of the WD procedure are shown in Fig. 4 for single beams (7, 22) in the period during the compression stroke from 200 to 340 °CA ATDC. A beam yielding high-quality data (typically characterised by high signal level), as shown in Fig. 4(a) and 4(b), is not significantly affected. However, application of WD to a poor-quality beam (typically characterised by low signal level), as shown in Fig. 4(c) and 4(d), allows robust assessment of the crank angle variation of the signal. In the latter case, the example signal shown is seen to be reliable, when compared with other cases of low-signal-level beams where the ratiometric data after denoising may show oscillations to values as high as 1.5 and they are discarded prior to image reconstruction.

The optimised methodology for the complete data pre-processing flow is shown in Fig. 5. The reference crank angle interval θ_{ref} (as defined in Section 2) was set to the period of 200 to 220 ºCA;

9

the optical signals $S_{\lambda1}(t)$ and $S_{\lambda2}(t)$ were then normalised, for each cycle, to their average value in that period. The choice of θ_{ref} was based on empirical observation of data behaviour, with the above region yielding the most stable signal levels from cycle-to-cycle. These are the data used in the further analysis below.
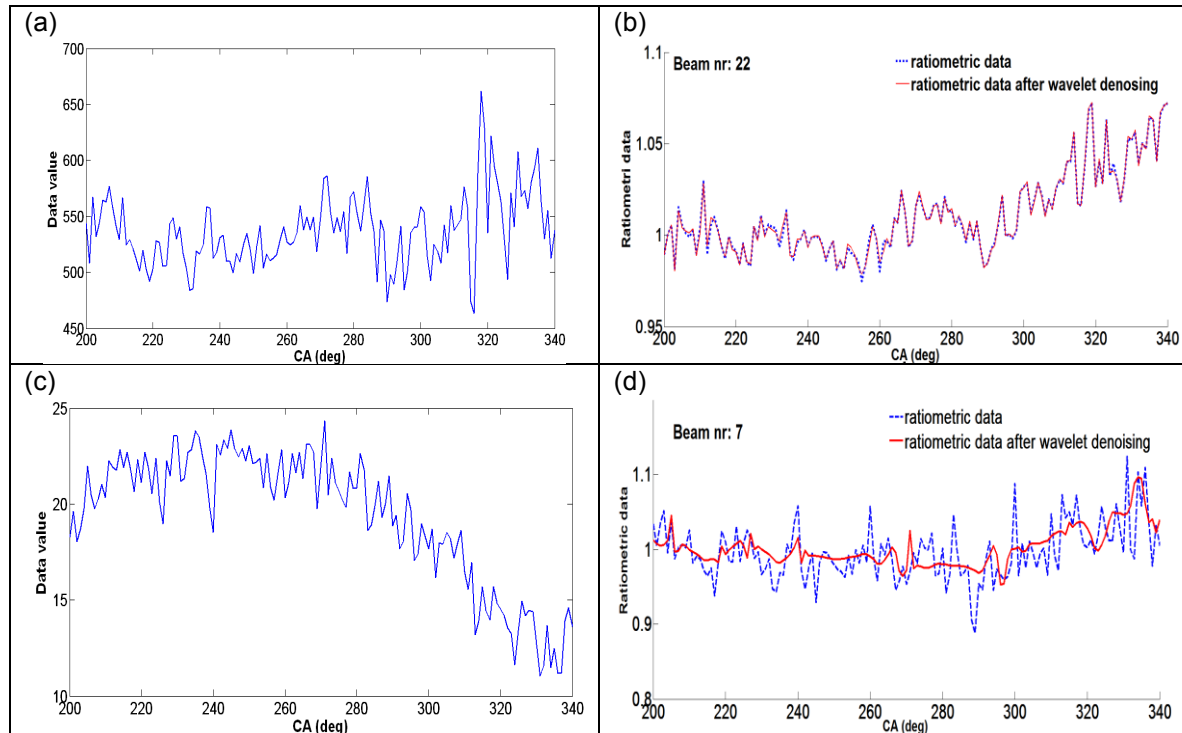

Figure 4: Examples of application of Wavelet Denoising (WD): (a) raw single-wavelength data indicating a high-quality beam (#22); (b) DWR data for beam 22 before and after WD; (c) raw single-wavelength data indicating a poor-quality beam (#7); (d) DWR data for beam 7 before and after WD.
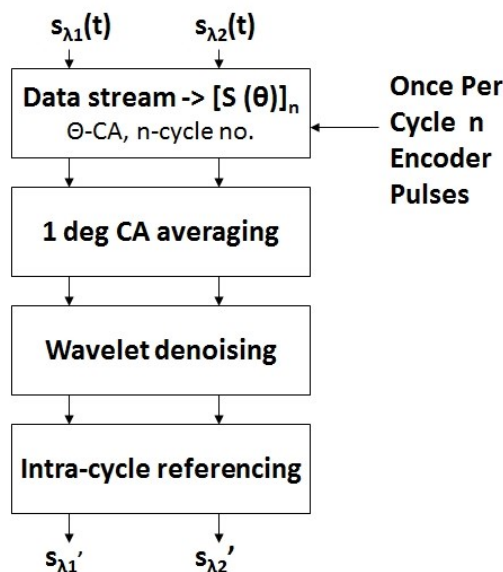

Figure 5: Flow diagram for data pre-processing.

Behaviour of ratiometric data

Figure 6(a) shows the ratios R_F and R_{UF} derived from the data of Fig. 3 (after denoising). Note the similar overall trends of both the fuelled and unfuelled ratios due to non-species-specific effects, such

10

as cylinder pressure variation during compression. Further improvements to the optical system are clearly very desirable, as discussed in section 7. Figure 6(b) shows, for the data of Fig. 6(a), the ratio R_F/R_{UF}, which isolates the attenuation due to the hydrocarbon fuel only, according to equ. (7). The reduction of this quantity as the compression proceeds is consistent in nature with that expected from the increasing average fuel concentration per unit volume, c. For iso-octane/air mixtures, it has been shown previously [21, 23] that the absorption coefficient, k, is a function of pressure, and hence of crankangle, θ. In the case of pure iso-octane fuel, the recorded in-cylinder pressure, also plotted in Fig. 6(b), can be used to calculate $k(\theta)$, using the calibration data of [21]. However, no such calibration data has been obtained for the fuel mixture used here.

For illustrative purposes only, it is worthwhile to carry out some calculations under the assumption that the fuel is pure iso-octane, which will create a systematic error in the estimate of the true fuel concentration since 3-pentanone molecules have many fewer C-H bonds than iso-octane molecules, and hence a lower k value at 1700 nm. Thus, under this assumption, the ratio shown in Fig. 6(b) implies a path-averaged concentration c_F of 0.0013 mol.l^{-1} at 320 $^\circ$CA. Using the same procedure for 5 beams at various orientations through the cylinder (selected to be representative of the cross-section), the mean value of all 5 path-averaged concentrations at 320 $^\circ$CA is found to be 0.0015 mol.l^{-1}, which is approximately 15% greater than the mean concentration measured at the same crank-angle position by Wright et al. [5] in a firing multi-cylinder engine with a stoichiometric mixture of pump grade fuel. An increased concentration would be expected in the present work, due to the non-firing operation of the engine and the negative valve overlap condition that results in increased trapping of residual fuel vapour within the cylinder.

Figs. 4(b), (d) and 6(b) demonstrate substantial short-term (1 – 5 $^\circ$CA) variations of the DWR values, relative to the degree of absorption attributable to fuel. There are a number of possible causes of these variations, such as beam steering due to spatial variations in refractive index of the mixing fuel/air charge, and variation of the measurand, i.e. the spatial distribution of fuel concentration. In order to examine the general temporal development of the fuel distribution, it was decided to average the DWR data over intervals of 3 $^\circ$CA, for each beam, prior to image reconstruction; this procedure was also followed in [5].
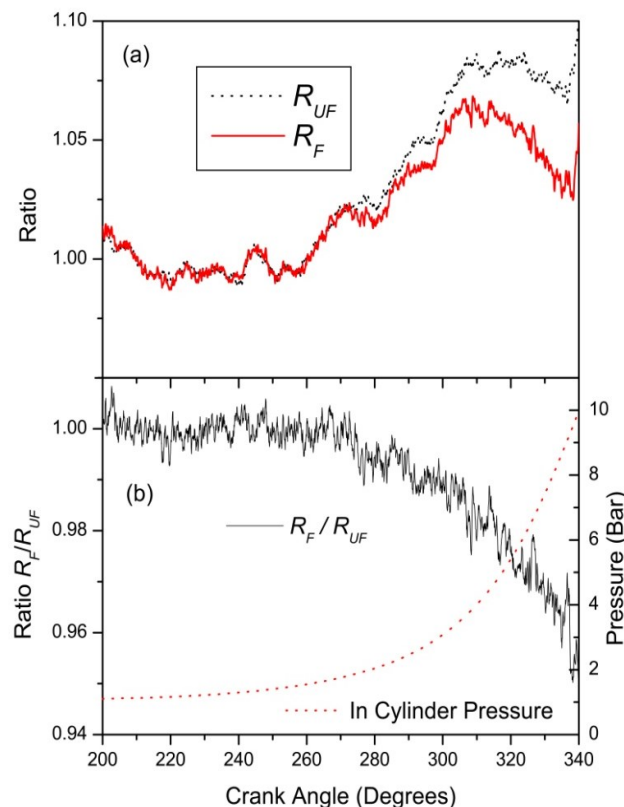

Figure 6: For the beam marked * in Figure 2, (a) DWR signals during the compression stroke, for both fuelled and unfuelled operation, and (b) the ratio of the data in (a).

6   Image reconstruction

Beam selection

In the analysis procedure, a qualification test was applied to each of the single-beam data prior to image reconstruction. In the case of spray imaging, the data used are those for the reference wavelength only; for vapour imaging, the data used are the ratio R_F/R_{UF}, as exemplified in Fig. 6(b). This qualification test prevents the resulting image being impaired by the inclusion of poor quality data, e.g., those with unacceptably low signal-to-noise ratio (SNR). The qualification test rejects beams according to the following criteria: the data show more than 5% peak-to-peak noise, or they exhibit physically implausible behaviour, e.g., ratiometric transmission showing values above 1.005. For the spray imaging data shown here, 28 beams (from 32 in total) satisfied the qualification test, and for the vapour imaging case 30 beams satisfied it. Schematic representations of the data processing steps are shown in Fig. 7.

$[s_{\lambda 1}(\theta)]_{nF}$ $[s_{\lambda 2}(\theta)]_{nF}$ $[s_{\lambda 1}(\theta)]_{nUF}$ $[s_{\lambda 2}(\theta)]_{nUF}$

$[s_{\lambda 1}(\theta)]_{nF} / [s_{\lambda 2}(\theta)]_{nF}$ $Avrg([s_{\lambda 1}(\theta)]_{nUF} / [s_{\lambda 2}(\theta)]_{nUF})$

$[s_{\lambda 2}(\theta)]_n$

Ratio of un-fuelled and fuelled cycles

Beam selection

Beam selection

Image reconstruction

Image reconstruction
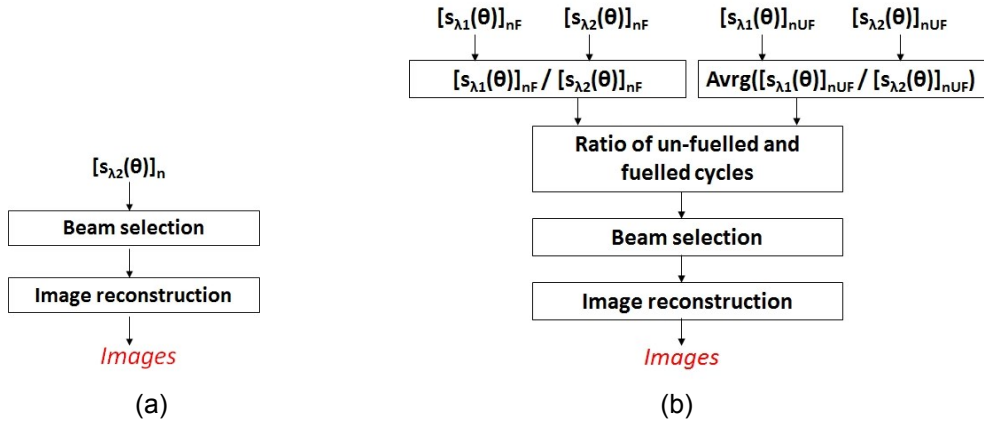
Images

Images

(a)

(b)

Figure 7: Flow diagram for data processing and tomographic image reconstruction for spatial distributions of (a) liquid fuel spray and (b) fuel vapour.

In order to assess the impact upon the images of the particular missing beams in each case, Fig. 8 shows the results of simulation with a homogeneous fuel distribution of normalised concentration value 1. The reconstructed distributions are shown along the bottom row of the figure, in a 3-dimensional view which happens in this particular case to show more clearly the effect of the missing beams in Figs. 8(b) and 8(c), relative to Fig. 8(a), because the missing beams are all located towards the inlet valve side of the cylinder.

When all 32 beams are used, Fig. 8(a) shows that the reconstructed distribution is quite flat and that the range of the reconstructed concentration values between pixels (called here the concentration variation, CV) within the reconstructed image is only 11%. The fact that the maximum reconstructed concentration is not equal to 1 is a systematic feature of the reconstruction algorithm and the sparse beam array. We do not apply to the engine data a global correction for that effect, since it depends upon our prior knowledge that the concentration distribution in the simulation case is homogeneous, and the use of prior information in tomographic image reconstruction is a matter for great care. CV worsens to 22% for the 30-beam case (Fig. 8(b)), with the variation running systematically from high concentration on the exhaust side, to low on the intake side. It worsens further to 48% for the 28-beam case (Fig. 8(c)), again running systematically in the same direction. Neither the 30-beam nor the 28-beam case shows any significant distortion in the direction perpendicular to the exhaust-inlet axis. It should be noted that the exhaust-to-inlet axis runs from top to bottom in all the plan view figures in this paper.
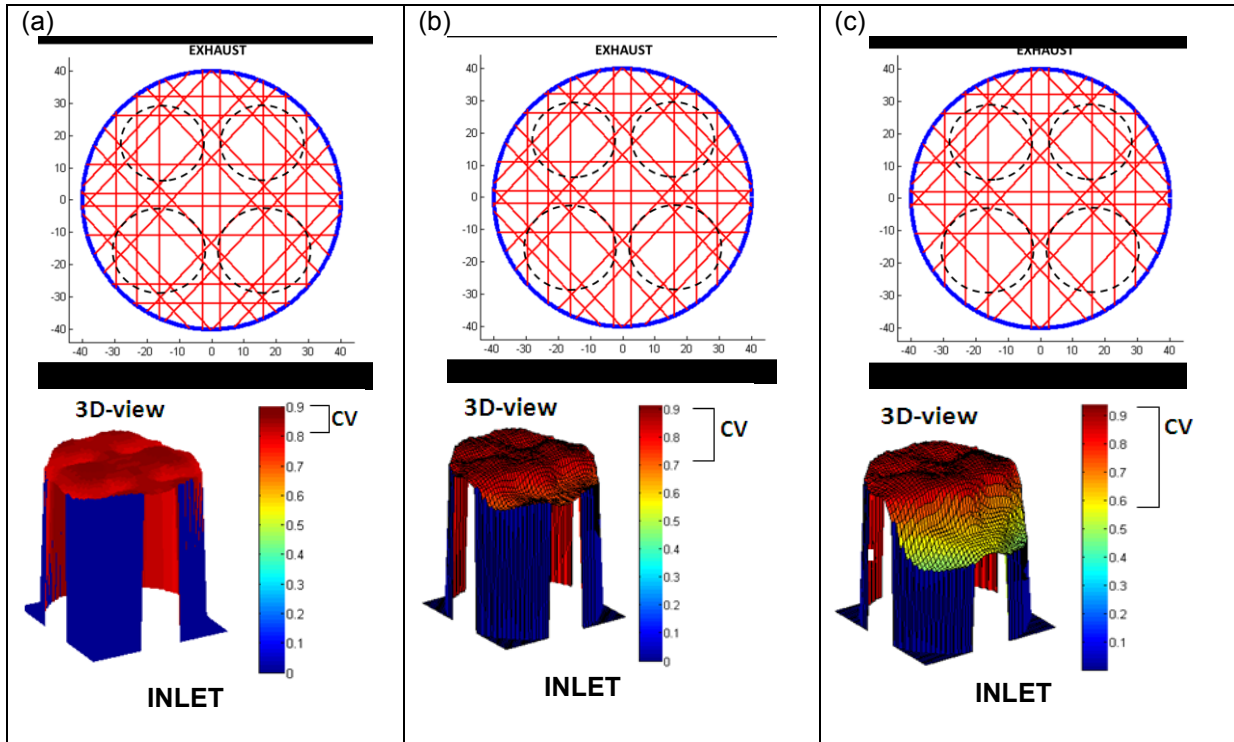
Figure 8: Reconstructed images (shown along the bottom row) for simulated measurements of a homogeneous distribution of fuel for: (a) the 32-beam array shown in the upper part of the figure (where the outlines of the 4 valves are also shown), showing 11% concentration variation (CV) in the reconstructed image; (b) the 30-beam array in the upper figure, showing 22% CV, and (c) the 28-beam array in the upper figure, showing 48% CV.

In all of the work presented here, the resulting datasets belong to a category of systems with severely limited data, in which both the number of viewing angles and the number of measurements are small. Image reconstruction in such situations is typically reliant upon the availability of some prior knowledge of the form of the subject. The image reconstruction algorithm used here is based on an enhanced iterative Landweber method. Previous work by the authors [23, 24] has shown that this method performs well in dealing with the severely limited data problem; it provides generality and can be modified in order to take into account additional *a priori* information about the solution, such as smoothness of the subject and value constraints within each iteration. In the work reported here, we used the median filter as a smoothing filter. A non-negativity constraint was also applied to maintain physically meaningful concentrations. We used a fixed number of iterations (set to 25) to stop the iteration process.

Figure 9 shows images of the relative fuel spray droplet concentration, in the plane of observation, at two crankangle points during the injection period, reconstructed from the engine data, for every other engine cycle, numbered 5, 7, 9 and 11 during a fuelled sequence. In the work presented here, using attenuation of only the reference wavelength λ_2 for spray imaging, no access was available to the detailed injector properties, and hence the data presented here are not calibrated to provide absolute liquid mass distributions. However, within each single image, and from image to image, the relative "concentration" values are quantitatively meaningful. At a fixed crankangle, the major features of the in-cylinder distributions are seen to be reproducible from cycle to cycle. The dynamical nature of the combined injection/flow process is evident from the marked changes in the distribution from 143 ºCA in Fig. 9(a) to 159 ºCA in Fig. 9(b), which are easily resolved in time by the tomography system presented here, with 1 frame per ºCA. There is a clear exhaust-inlet asymmetry that is partly a result of the missing beams, as noted in the simulation results (Fig. 8(c) above), but is much greater than the effect due to the missing beams. However, there is also a persistent asymmetry from cycle-to-cycle in the direction perpendicular to the exhaust-inlet axis: there is a greater concentration of scattering 'centres' (attributed to spray droplets) in the right half of the cylinder at 143 ºCA in Fig. 9(a), which is reversed at 159 ºCA in Fig. 9(b).
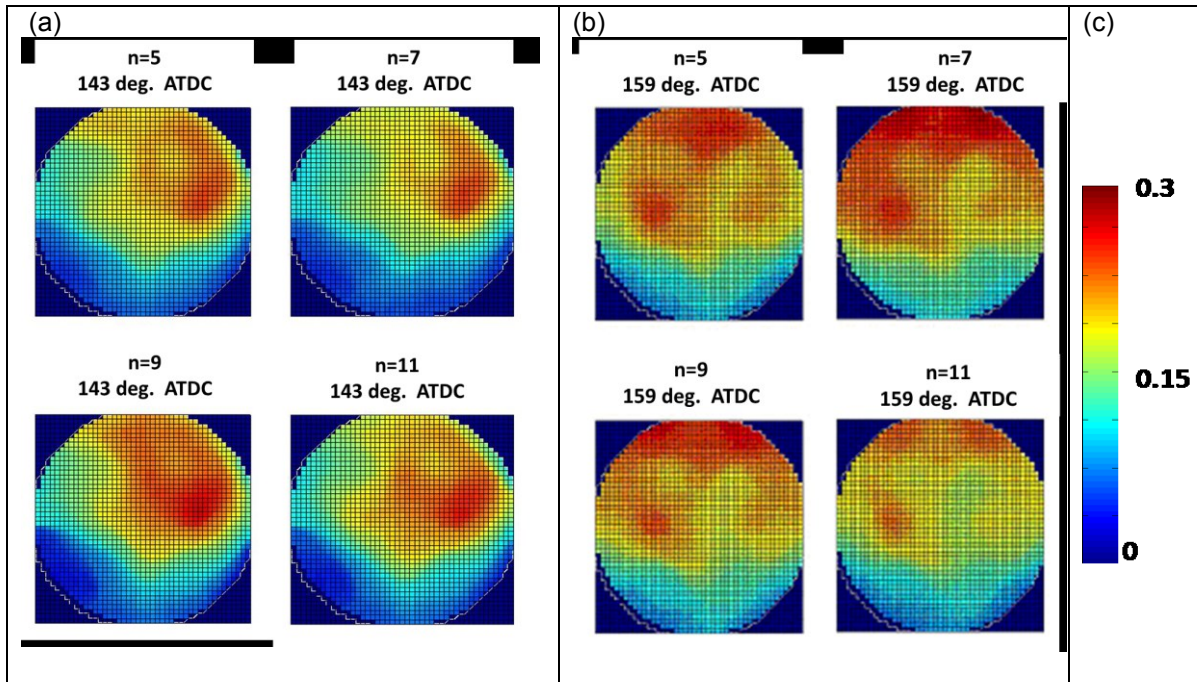
Figure 9: Typical reconstructed distributions of liquid fuel spray in four engine cycles, each cycle numbered (n) within a single fuelled sequence, at given crank angles after exhaust Top Dead Centre(=0 ºCA), (a) at 143 ºCA, and (b) at 159 ºCA. The colour scale (arbitrary units) is shown in part (c), and is fixed for all images in this Figure.

In principle, the CST technique yields quantitative images of fuel distribution, as discussed in section 2 and demonstrated in [5, 23]. However, the absence of calibration data, i.e. $k(\theta)$, for the fuel mixture used in the present study prevents quantification of CST images here. Figure 10 shows CST images of the relative fuel vapour concentration, in the plane of observation, for the late compression period, for consecutive engine cycles 9 to 12 during a fuelled sequence. The colour scale is consistent between all images. Each row shows the evolution of the relative vapour distribution within a single compression stroke, at intervals of 3 ºCA, and each column shows the cycle to cycle variation at a fixed crankangle. The images show a relatively smooth variation of fuel vapour distribution within a single compression stroke. The variation from cycle-to-cycle, at a fixed crankangle, appears to be small. Again, there is a persistent exhaust-inlet asymmetry, but now very much greater than that due to the two missing beams (as shown in Fig. 8(b) above), showing a much higher concentration of fuel vapour towards the exhaust side of the cylinder. In this case also there is a persistent asymmetry in the direction perpendicular to the exhaust-inlet axis, with greater fuel concentration in the right half of the cylinder.

The images in Figs. 9 and 10 show, for each of the individual engine cycles numbered 9 and 11, the in-cylinder distribution of, firstly, the spray droplets during/immediately after fuel injection, and secondly, the HC fuel vapour during compression. This is the first time that the spatial evolution of the fuel charge within a plane of the cylinder has been measured by tomographic imaging techniques, from liquid spray injection to vapour behaviour in the late compression stroke, during single cycles and over consecutive cycles of an internal combustion engine.
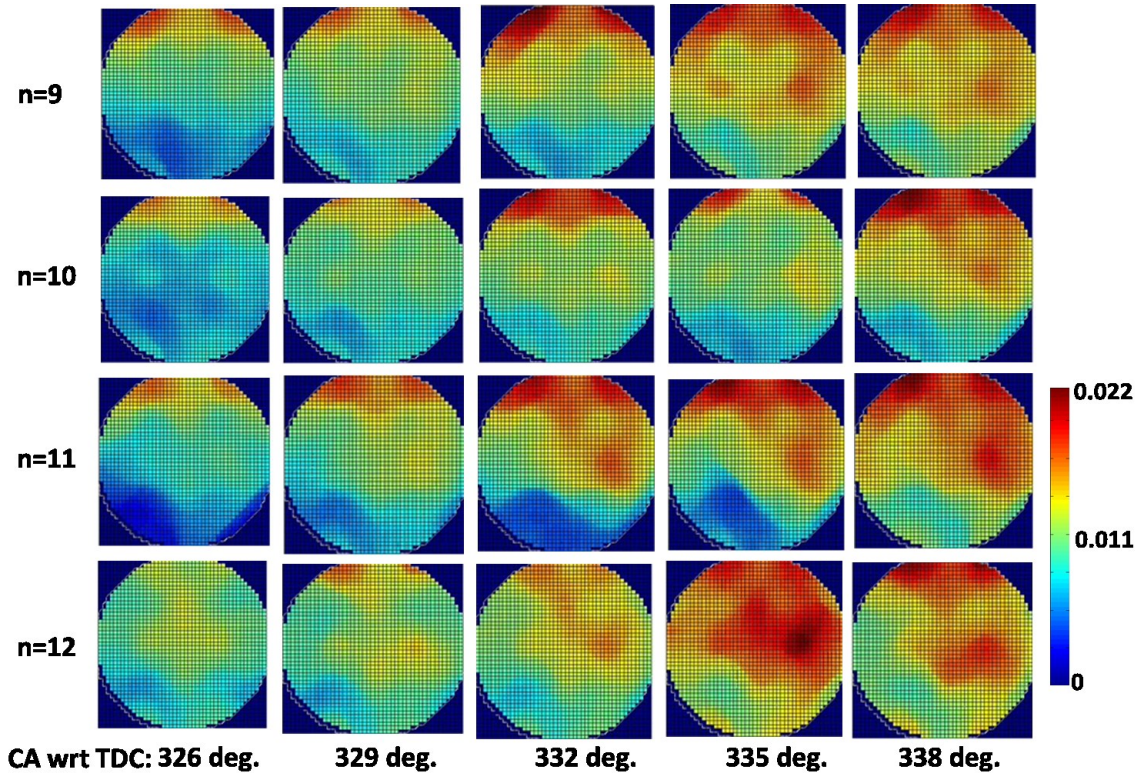
14

Figure 10: Typical reconstructed distributions of fuel vapour in four consecutive engine cycles, each numbered (n) within a single fuelled sequence, at given crank angles after exhaust Top Dead Centre (=0 ºCA). Each row shows the vapour distribution within a single compression stroke, at intervals of 3 ºCA, and each column shows the cycle-to-cycle variation at a fixed crankangle. The colour scale (arbitrary units) is shown at the far right, and is fixed for all images in this Figure.

7   DISCUSSION AND CONCLUSIONS

Acquisition of good-quality data for in-cylinder optical tomography in a single-cylinder optical engine has been facilitated by a simple new opto-mechanical approach, based on accurately machined V-grooves in a flat metallic plate, giving satisfactory optical alignment for up to 32 beams. The signal behaviours in Figs. 4(b), 4(d) and 6(a), where the DWR in the compression stroke is seen to increase with θ, are due mainly to a combination of refractive effects as the in-cylinder pressure increases, non-identical beam profiles of the two launched wavelengths along each path, and cyclical vibration effects. Improved optical design could reduce these effects. Nevertheless, with less than 10% deviation of these signals above unity in the present study, these imperfections are readily dealt with by referencing to unfuelled cycles. The success of this procedure is shown by the example data for the ratio (R_F/R_{UF}) in Fig. 6(b), and the equivalent data are typically well-behaved for all beams in the present study. It is worthwhile to note that, in the fired multi-cylinder engine study described in [5], physical distortion of the cylinder was a major contributor to data equivalent to Figs. 4(b), 4(d) and 6(a) deviating above unity by as much as 50%. Assessment of beam data quality was further assisted by a Wavelet Denoising process which maximised the retention of beams, a feature of central importance for robust tomography.

In a motoring internal combustion engine, in the same engine cycle, the first in-cylinder tomographic images have been obtained of the cross-sectional distribution of liquid fuel spray droplets during and immediately after direct injection, followed by cross-sectional images of hydrocarbon fuel vapour distribution during compression. The spatial distribution of the liquid fuel spray was imaged at 7,200 fps by using only the attenuation of the reference wavelength. Image reconstruction of Dual-Wavelength Ratio (DWR) data provided fuel vapour images at 2,400 fps in the compression stroke. The intra-cycle large-scale temporal dynamics of the spray are revealed to be particularly marked, whilst the variation of the vapour distribution during the compression stroke is relatively smooth.

15

As shown by the simulations presented in Fig. 8, the observed asymmetry of fuel distribution (Figs. 9 and 10) perpendicular to the exhaust-inlet axis is not due to any bias imposed by the beam array, nor is it due to data selection or subsequent processing. Moreover, the rapid temporal variations observed in the spray period clearly show that this asymmetry is due to the spray process and in-cylinder flow dynamics, which further strengthens the view that the asymmetries observed during the late compression period are also due entirely to the nature of the fuel/air flow and mixing processes. The observed asymmetry of fuel distribution along the exhaust-inlet axis in Figs. 9 and 10 is much greater than that expected due to the missing beams (Fig. 8).

In a very similar engine with comparable geometry and valve strategies, the motored air motion in the mid-cylinder plane was characterised in a previous study [29] using Particle Image Velocimetry (PIV) via a Bowditch piston. Measurements were taken during the intake stroke, with conventional intake and exhaust valve timings and peak valve lift (9 mm), as well as NVO timings and a reduced peak lift (2.3 mm). The results revealed a rotating air motion: the coherent tumbling structures in the intake stroke became distorted and broke down during the compression stroke. Towards the end of the stroke, disordered, smaller scale motions were observed, unevenly distributed about the cylinder's vertical axis of symmetry, until a characteristic piston driven flow was observed close to TDC (firing). Hence, the asymmetrical fuel distribution effects observed in the present study are not unexpected: in general, the forward tumble motion has deflected the central fuel cloud towards the exhaust side of the cylinder.

The work reported here did not include fired operation and did not assess the long-term robustness of operation of the system, e.g., in terms of fouling of optical surfaces. However, the previous implementation of this CST system [5] on a multi-cylinder production engine, running on pump grade fuel, still yielded good quality data after 2 hours of fired operation. Hence, extension of the present work to fired operation of single-cylinder optical engines is anticipated. Experimental validation of the in-cylinder fuel distributions obtained by tomography (in addition to reported laboratory validations, e.g., [6, 23, 24]) remains as a future objective, most probably by using PLIF. Subject to that proviso, the results obtained here promise that optical tomography and CST will provide, for some R&D studies, penetrating spatial and temporal information on in-cylinder fuel distributions, with the freedom to use a wide variety of fuels. Simply by opto-electronic development, extensions of the method to other in-cylinder species, such as water [30] and CO [31], are important medium-term targets.

8 ACKNOWLEDGEMENTS

9 REFERENCES

[1] Ch. Schwarz, E. Schünemann, B. Durst, J. Fischer, A. Witt, Potentials of the spray-guided BMW DI combustion system, SAE Paper No. 2006-01-1265, 2006.

[2] H. Baecker, A. Kaufmann, M. Tichy, Experimental and simulative investigation on stratification potential of spray-guided GDI combustion systems, SAE Paper No. 2007-01-1407, 2007.

[3] K.H. Lee, C.H. Lee, Experimental Thermal and Fluid Science **31** (2007) 579-592, DOI:10.1016/j.expthermflusci.2006.06.003.

[4] B. Thirouard, J. Cherel, Nature of CAI combustion and air/fuel ratio stratification effects, Oil & Gas Science and Technology – REV. IFP, 2006.

16

[5]   P. Wright, N. Terzija, J.L. Davidson, S. Garcia-Castillo, C.A. Garcia-Stewart, S. Pegrum, S. Colbourne, P. Turner, S.D. Crossley, T.J. Litt, S.C. Murray, K.B. Ozanyan, H. McCann, Chem. Eng. J. **158** (2010) 2-10 DOI:10.1016/J.CEJ.2008.10.026.

[6]   F.P. Hindle, S.J. Carey, K.B. Ozanyan, D.E. Winterbone, E. Clough, H. McCann, Technisches Messen **69** (2002) 352-357, DOI:10.1524/TEME.2002.69.7-8.352.

[7]   S.N. Soid and Z.A. Zainal,   Energy **36** (2011) 724 – 741

[8]   C. Schulz and V. Sick, Prog. Energy Combust. Sci. **31** (2005) 75-121.

[9]   V. Sick, Proc. Comb. Inst. **34** (2013) 3509-3530

[10]   J. Hult, M. Richter, J. Nygren , et al., Appl. Opt. **41** (2002) 5002-5014

[11]   W. Hentschel, B. Block, T. Hovestadt, G. Ohmstede, V. Richter, et al., SAE (2001) 2001-01-3648

[12]   K. Nishida, J. Tian, Y. Sumoto, et al., Fuel **88** (2009) 1634–1642

[13]   T. Fang, R.E. Coverdill, C. F. Lee, and R.A. White, Fuel **87** (2008) 3232-3239

[14]   V. Sick, M.C. Drake and T.D. Fansler, Exp Fluids **49** (2010) 937–947, DOI: 10.1007/s00348-010-0891-3

[15]   L.A. Melton, Appl. Optics **22** (1983) 2224–2226.

[16]   R. Shimizu, S. Matumoto, S. Furuno, S., M. Murayama, and S. Kojima, SAE paper 922356, 1992.

[17]   B. Leach, H. Zhao, Y. Li, T. Ma, Proc. IMechE Vol. 221 (2007) Part D: J. Automobile Eng. 663-673, DOI: 10.1243/09544070JAUTO305.

[18]   T.D. Fansler, M.C. Drake, B. Gajdeczko, I. Duwel, W. Koban, F.P. Zimmermann and C. Schulz, Meas. Sci. Technol. **20** (2009) 125401 (13pp) doi:10.1088/0957-0233/20/12/125401

[19]   J.M. Whitney, K. Takami, Kuya; S.T. Sanders, et al., IEEE Sensors Journal **11** (2011) 3295-3302 DOI: 10.1109/JSEN.2011.2156780

[20]   M. Bertero and P. Boccacci, Introduction to Inverse Problems in Imaging (2nd edition), 2010, CRC Press

[21]   P. Wright, K.B. Ozanyan, C.A. Garcia-Stewart, S.J. Carey, F.P. Hindle, W. Hurr, S. Pegrum, S. Colbourne, P. Turner, S.D. Crossley, T. Litt, S.C. Murray, H. McCann, Appl. Optics **44** (2005) 6578-6592, DOI:10.1364/AO.44.006578.

[22]   X. Liu, X. Zhou, J.B. Jeffries, R.K. Hanson, (2007), J. Quant. Spectr. & Rad. Trans., 103, 565-577

[23]   N. Terzija, J.L. Davidson, C.A. Garcia-Stewart, P. Wright, K.B. Ozanyan, S. Pegrum, T.J. Litt, H. McCann, Meas. Sci. Technol. **19** (2008) 094007, doi:10.1088/0957-0233/19/9/094007.

[24]   N. Terzija, H. McCann, IEEE Sensors J. **11** (2011) 1885-1893 doi:10.1109/JSEN.2010.2100378.

[25]   D.L. Donoho, IEEE Transactions on Information Theory **41** (1995) 613-627.

[26]   D.L. Donoho, I.M. Johnstone, G. Kerkyacharian, D. Picard, J. Royal Statistical Society B. **57** (1995) 301-337.

[27]   I. Daubechies, Ten Lectures on Wavelets, Society for Industrial and Applied Mathematics, Philadelphia, PA, 1992.

[28]   D.L. Donoho, I.M. Johnstone, Biometrika **81** (1994) 425-455.

[29]   S. Begg, D. Mason, M. Heikal, Spark Ignition And Spark-Assisted Controlled Auto-Ignition In An Optical Gasoline Engine. SAE/JSAE Technical Paper Series 2009-32-0072/20097072, 15th Small Engine Technology Conference (Setc), Penang, Malaysia, 2009.

[30]   S. Karagiannopoulos, E.M. Cheadle, P. Wright, S.A. Tsekenis, and H. McCann, Appl. Opt. **51** (2012), 8057–8067 doi:10.11364/AO.51.008057

[31]   S. Pal and H. McCann, Meas. Sci. Technol. **22** (2011) 115304 (13 pp) doi:10.1088/0957-0233/22/11/115304

FIGURE CAPTIONS:

Figure 1: Schematic of the optical liner installation, (a) section view, and (b) perspective view.

Figure 2: Plan view of 32-beam array mounted on the engine showing grooved plate and beam paths relative to intake and exhaust ports and camshaft (* denotes the example beam referred to in Figs. 3, 6, i.e. the vertical beam immediately to the left of the * symbol).

Figure 3: Average recorded signal intensity for 16 fuelled cycles for the selected example beam (reference wavelength) during the intake and compression strokes and engine cycle events.

Figure 4: Examples of application of Wavelet Denoising (WD): (a) raw single-wavelength data indicating a high-quality beam (#22); (b) DWR data for beam 22 before and after WD; (c) raw single-wavelength data indicating a poor-quality beam (#7); (d) DWR data for beam 7 before and after WD.

Figure 5: Flow diagram for data pre-processing.

Figure 6: For the beam marked * in Figure 2, (a) DWR signals during the compression stroke, for both fuelled and unfuelled operation, and (b) the ratio of the data in (a).

Figure 7: Flow diagram for data processing and tomographic image reconstruction for spatial distributions of (a) liquid fuel spray and (b) fuel vapour.

Figure 8: Reconstructed images (shown along the bottom row) for simulated measurements of a homogeneous distribution of fuel for: (a) the 32-beam array shown in the upper part of the figure (where the outlines of the 4 valves are also shown), showing 11% concentration variation (CV) in the reconstructed image; (b) the 30-beam array in the upper figure, showing 22% CV, and (c) the 28-beam array in the upper figure, showing 48% CV.

Figure 9: Typical reconstructed distributions of liquid fuel spray in four engine cycles, each cycle numbered (n) within a single fuelled sequence, at given crank angles after exhaust Top Dead Centre(=0 ºCA), (a) at 143 ºCA, and (b) at 159 ºCA. The colour scale (arbitrary units) is shown in part (c), and is fixed for all images in this Figure.

Figure 10: Typical reconstructed distributions of fuel vapour in four consecutive engine cycles, each numbered (n) within a single fuelled sequence, at given crank angles after exhaust Top Dead Centre (=0 ºCA). Each row shows the vapour distribution within a single compression stroke, at intervals of 3 ºCA, and each column shows the cycle-to-cycle variation at a fixed crankangle. The colour scale (arbitrary units) is shown at the far right, and is fixed for all images in this Figure.